nature genetics

LETTERS

https://doi.org/10.1038/s41588-018-0166-0

Biallelic loss of human *CTNNA2*, encoding αN-catenin, leads to ARP2/3 complex overactivity and disordered cortical neuronal migration

Ashleigh E. Schaffer[1,2*], Martin W. Breuss[1], Ahmet Okay Caglayan[3,4], Nouriya Al-Sanaa[5], Hind Y. Al-Abdulwahed[5], Hande Kaymakçalan[6], Cahide Yılmaz[7], Maha S. Zaki[8], Rasim O. Rosti[1], Brett Copeland[1], Seung Tae Baek[1], Damir Musaev[1], Eric C. Scott[1], Tawfeg Ben-Omran[9], Ariana Kariminejad[10], Hulya Kayserili[11], Faezeh Mojahedi[12], Majdi Kara[13], Na Cai[1], Jennifer L. Silhavy[1], Seham Elsharif[13], Elif Fenercioglu[14], Bruce A. Barshop[15], Bulent Kara[16], Rengang Wang[1], Valentina Stanley[1], Kiely N. James[1], Rahul Nachnani[1], Aneesha Kalur[2], Hisham Megahed[8], Faruk Incecik[17], Sumita Danda[18], Yasemin Alanay[19], Eissa Faqeih[20], Gia Melikishvili[21], Lobna Mansour[22], Ian Miller[23], Biayna Sukhudyan[24], Jamel Chelly[25], William B. Dobyns[26], Kaya Bilguvar[3], Rami Abou Jamra[27], Murat Gunel[3] and Joseph G. Gleeson[1*]

Neuronal migration defects, including pachygyria, are among the most severe developmental brain defects in humans. Here, we identify biallelic truncating mutations in *CTNNA2*, encoding αN-catenin, in patients with a distinct recessive form of pachygyria. *CTNNA2* was expressed in human cerebral cortex, and its loss in neurons led to defects in neurite stability and migration. The αN-catenin paralog, αE-catenin, acts as a switch regulating the balance between β-catenin and Arp2/3 actin filament activities[1]. Loss of αN-catenin did not affect β-catenin signaling, but recombinant αN-catenin interacted with purified actin and repressed ARP2/3 actin-branching activity. The actin-binding domain of αN-catenin or ARP2/3 inhibitors rescued the neuronal phenotype associated with *CTNNA2* loss, suggesting ARP2/3 de-repression as a potential disease mechanism. Our findings identify *CTNNA2* as the first catenin family member with biallelic mutations in humans, causing a new pachygyria syndrome linked to actin regulation, and uncover a key factor involved in ARP2/3 repression in neurons.

The lissencephaly (LIS) spectrum is characterized by defects in the folding pattern of the cerebral cortex, resulting in reduced numbers or complexity of gyri that characterize the human brain[2]. LIS encompasses a continuum of malformations ranging from complete agyria to pachygyria, in which gyral formation is diminished but not absent. Patients present clinically with failed motor and cognitive development followed by intractable epilepsy. Most patients are severely intellectually impaired, and are unable to walk or care for themselves.

Projection neurons of the cerebral cortex are born in a zone adjacent to the ventricle, then migrate to the future six-layered neocortex. Neuronal migration is achieved through a rearrangement of cytoskeletal components in response to extracellular cues, mediated by numerous intracellular signaling pathways[3]. Coordinated regulation of monomeric (G-actin) and polymerized actin microfilaments (F-actin) is critical for neuronal growth cone morphogenesis, axon pathfinding, and neurite extension during migration[4,5]. Positive regulators of F-actin assembly include families of nucleating proteins (formins and Arp2/3) and their co-activators (Rho GTPases, and

---

[1]Department of Neuroscience, Rady Children's Institute for Genomic Medicine, Howard Hughes Medical Institute, University of California, San Diego, San Diego, CA, USA. [2]Department of Genetics and Genome Sciences, Case Western Reserve University, Cleveland, OH, USA. [3]Departments of Neurosurgery, Neurobiology, and Genetics, Yale University School of Medicine, New Haven, CT, USA. [4]Department of Medical Genetics, Istanbul Bilim University, Istanbul, Turkey. [5]Department of Pediatrics, Johns Hopkins Aramco Healthcare, Dhahran, Saudi Arabia. [6]Department of Pediatrics, Istanbul Bilim University, Istanbul, Turkey. [7]Department of Pediatrics, Yıldırım Beyazıt University, Ankara, Turkey. [8]Clinical Genetics Department, Human Genetics and Genome Research Division, National Research Centre, Cairo, Egypt. [9]Clinical and Metabolic Genetics Section, Department of Pediatrics, Hamad Medical Corporation, Doha, Qatar. [10]Kariminejad-Najmabadi Pathology and Genetic Center, Tehran, Iran. [11]Department of Medical Genetics, Koç University School of Medicine, Istanbul, Turkey. [12]Mashhad Medical Genetic Counseling Center, Mashhad, Iran. [13]University of Tripoli, Tripoli Children's Hospital, Tripoli, Libya. [14]L.E.S. Mikrogen Genetic Diseases Diagnosis Center, Istanbul, Turkey. [15]Department of Pediatrics, Biochemical Genetics Program, University of California, San Diego, San Diego, CA, USA. [16]Department of Pediatric Neurology, Kocaeli University, Kocaeli, Turkey. [17]Department of Pediatric Neurology, Cukurova University, Adana, Turkey. [18]Department of Clinical Genetics, Christian Medical College and Hospital, Vellore, India. [19]Pediatric Genetics Unit, Department of Pediatrics, Acibadem Mehmet Ali Aydinlar University, Istanbul, Turkey. [20]Section of Medical Genetics, Department of Pediatrics, King Fahad Medical City, Children's Hospital, Riyadh, Saudi Arabia. [21]Department of Pediatrics, MediClubGeorgia, Tbilisi, Georgia. [22]Pediatric Department, Neuropediatric Unit, Cairo University Children's Hospital, Cairo, Egypt. [23]Neurology Department, Nicklaus Children's Hospital, Miami, FL, USA. [24]Arabkir Joint Medical Center and Institute of Child and Adolescent Health, Yerevan, Armenia. [25]Institut Cochin, Université Paris-Descartes, CNRS (UMR 8104), Paris, France. [26]Departments of Pediatrics and Neurology, University of Washington, Seattle, WA, USA. [27]Institute of Human Genetics, University of Leipzig Hospitals and Clinics, Leipzig, Germany. *e-mail: ashleigh.schaffer@case.edu; jogleeson@ucsd.edu

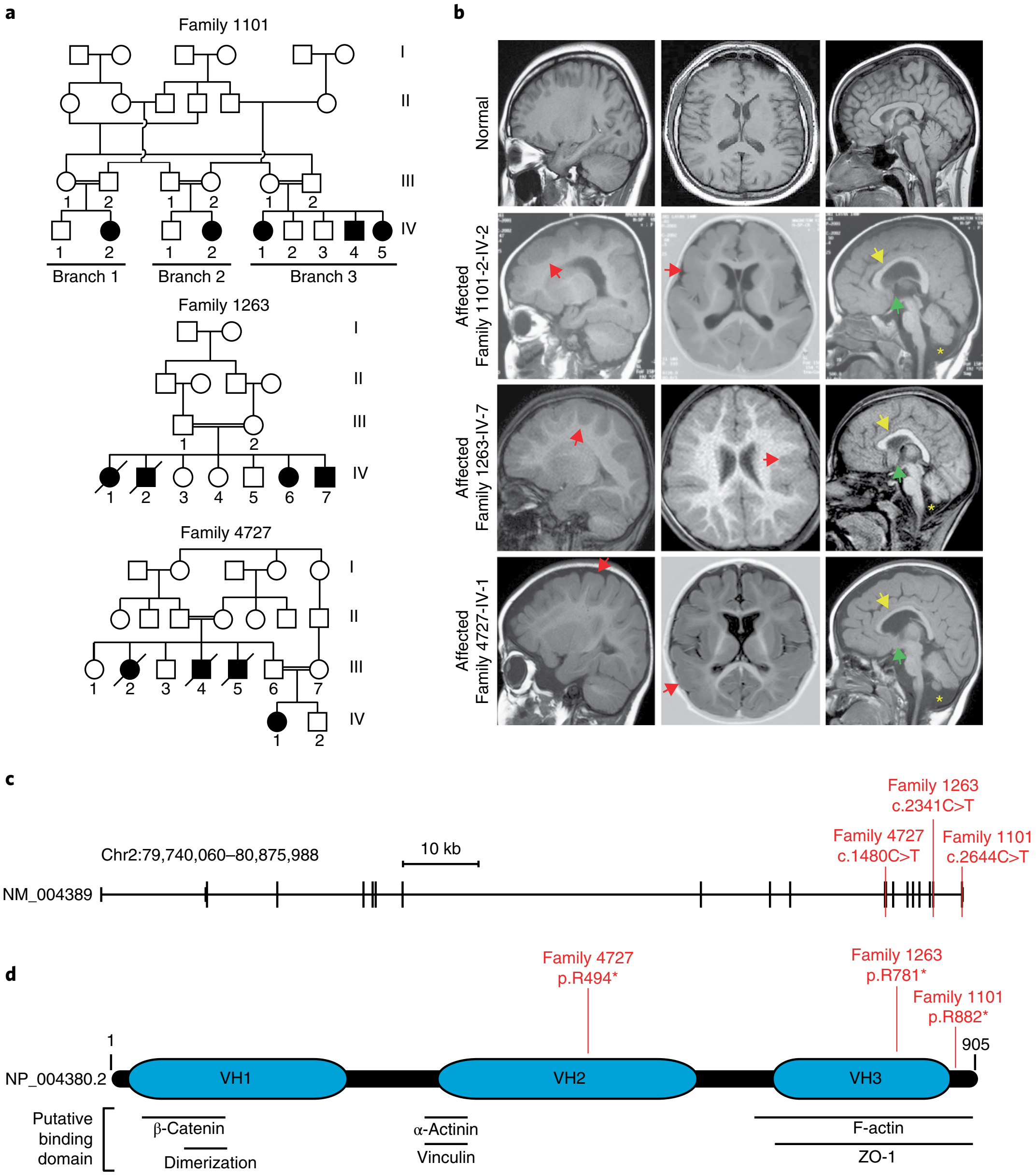

Fig. 1 | Identification of homozygous truncating *CTNNA2* mutations in families with pachygyria. a, Pedigrees of three consanguineous families. A double bar represents parental consanguinity. All living individuals in the last two generations were sampled. Males are represented by squares, females by circles and affected individuals by shading. **b**, Sagittal (left), axial (middle), and midline sagittal (right) MRI images. Affected individuals have symmetrically thickened cortex (red arrowheads) and a paucity of cortical gyri, consistent with pachygyria. They also present with a thin corpus callosum (yellow arrowheads), an absent anterior commissure (green arrowheads), and a fluid cavity as a result of cerebellar hypoplasia (mega cisterna magna, yellow asterisks). **c**, *CTNNA2* genomic organization. The location of the mutations in families 1101, 1263, and 4727 are shown in red. **d**, CTNNA2 905 amino acid polypeptide (NP_004380.2) with vinculin homology domains (VH1–3) and putative protein binding sites. Patient homozygous truncating mutations in red. ZO-1, zonula occludens-1.

the Wiskott–Aldrich syndrome family proteins WASP and WAVE), but negative regulators remain elusive, particularly in neurons[6].

We recruited three families, with seven affected individuals showing neurodevelopmental delay (Fig. 1a and Table 1). All were diagnosed before the age of two years and displayed acquired microcephaly, hypotonic cerebral palsy, inability to ambulate or speak, and intractable seizures (Table 1). Magnetic resonance imaging (MRI) demonstrated pachygyria with dramatic cortical gray matter thickening up to 3–4 cm, with a paucity of gyri without an obvious posterior–anterior gradient or focal dysplasias. There was absent anterior commissure, hypogenesis of the corpus callosum, and cerebellar hypoplasia (Fig. 1b). This phenotype is distinct from *LIS1*-pachygyria or *DCX*-pachygyria, which show posterior or anterior gradients, respectively. All subjects were enrolled using Institutional Review Board-approved protocols and provided consent for the study. We performed whole-exome sequencing[7] on at least one member of each family[8]. We prioritized rare (<0.2% allele frequency) damaging variants (genomic evolutionary rate profiling score >4 or sorting intolerant from tolerant score <0.05) and focused on homozygous variants due to parental consanguinity. Parametric linkage analysis from genome-wide SNP arrays and homozygosity mapping[9,10] showed identical-by-descent haplotypes (Supplementary Fig. 1a). Aligning variants with corresponding homozygous intervals identified putative nonsense variants in

Table 1 | Clinical phenotypes

	Family 1101-1-IV-2	Family 1101-2-IV-2	Family 1101-3-IV-1	Family 1101-3-IV-4	Family 1263-1	Family 1263-2	Family 4727-IV-1
Gender	F	F	F	M	M	F	F
Origin	Saudi	Saudi	Saudi	Saudi	Turkish	Turkish	Saudi
Weight at birth (kg)	2.9	NA	NA	NA	2.7	2.5	3.5
Length at birth (cm)	46	NA	NA	NA	49	48	NA
HC at birth (cm)	35.5	NA	NA	NA	NA	NA	NA
HC at birth (s.d.)	0	NA	NA	NA	NA	NA	NA
HC at last examination (cm)	50	53.5	53	51	44	47	46.5
HC at last examination (s.d.)[a]	−4	−1/0	−1	−2/−1	−5	−5	−5
Diagnosis age	2 years	1.5 years	1 year	Birth	30 months	9 years	28 months
Intellectual disability	Severe	Severe	Severe	Severe	Severe	Severe	NA
Development							
Gross motor	Delayed	Delayed	Delayed	Delayed	Delayed	Absent	Delayed
Fine motor	Delayed	Delayed	Delayed	Delayed	Delayed	Absent	Delayed
Language	Single words	Single words	Single words	Absent	Absent	Absent	Absent
Social	Delayed	Delayed	Delayed	Delayed	Delayed	Absent	Delayed
Seizures							
Onset	2–3 years	1.5 years	6 months	3 years	8 months	6 months	6 months
Type	Variable-atonic	Atonic/myoclonic	Variable-atonic	Variable-atonic	Atonic/myoclonic	Atonic/myoclonic	Infantile spasm (hypsarrhythmia)
Frequency	1–2 wk^{-1}	1–2 wk^{-1}	1–2 wk^{-1}	1–2 wk^{-1}	Monthly	Monthly	NA
Neurological findings							
Hypertonia	–	–	–	–	–	–	+
Hypotonia	+	+	–	+	+	+	+ (truncal)
Deep tendon reflexes	Increased	Increased	–	Increased	Increased	Increased	Increased
Spastic tetraplegia	+	–	–	+	–	+	+
Ataxia	Non-ambulatory	+	+	Non-ambulatory	–	Non-ambulatory	Non-ambulatory
Investigations							
Metabolic	Normal	Normal	Normal	Normal	NA	NA	Negative
VEP/ERG	Normal	Normal	NA	Abnormal	NA	NA	NA
EEG	Abnormal	Abnormal	Abnormal	Abnormal	Abnormal	Abnormal	Abnormal
MRI							
LIS spectrum	Pachygyria	Pachygyria	Pachygyria	Pachygyria	Pachygyria	Pachygyria	Pachygyria
Cerebral mantle thickening (mm)[b]	9–30	12–35	10–30	10–32	12–22	9–24	9–35
Subcortical band heterotopia	–	–	–	–	–	–	–
Corpus callosum	NA	NA	Thin	Thin	Thin	Thin	Thin
Cerebellar hypoplasia	Yes	Yes	Yes	Yes	Yes	Yes	Yes
Brainstem hypoplasia	No	No	No	No	No	No	Yes
Hydrocephalus	No	No	No	No	No	NA	NA
White matter paucity	Yes	Yes	Yes	Yes	Yes	Yes	NA
White matter signal	NA	NA	NA	NA	NA	NA	NA
Miscellaneous							
Polyhydramnios	–	–	–	–	–	–	–
Lung hypoplasia	–	–	–	–	–	–	–
Short stature	–	–	–	–	–	–	–
Macrocephaly	–	–	–	–	–	–	–
Optic atrophy	–	–	–	–	–	–	–
Autistic features	+	+	+	+	+	+	+
Dysmorphism	–	–	–	–	B/L pes equinovarus	–	–

Patients display acquired microcephaly, hypotonic cerebral palsy, inability to ambulate or speak, and intractable seizures. [a]Standard deviation below the mean. [b]Normal is 5 mm. B/L, bi-lateral; HC, head circumference; EEG, electroencephalogram; ERG, electroretinogram; NA, not available; VEP, visual evoked potential.

CTNNA2 in all three families (family 1101: c.2664C>T, p.Arg882*; family 1263: c.2341C>T, p.Arg781*; family 4727: c.1480C>T, p.Arg494*) (Fig. 1c,d and Supplementary Fig. 1b). The three variants were each observed once, only heterozygous, in the public databases Exome Aggregation Consortium (ExAC) and Genome Aggregation Database (gnomAD). Sanger sequencing confirmed segregation according to a strict recessive mode of inheritance, with full penetrance, in all genetically informative available family members, suggesting that biallelic *CTNNA2* loss-of-function mutations underlie pachygyria in these patients.

CTNNA2 is the ancestral α-catenin gene and is conserved in all Metazoa, but is predominantly expressed in the brain in mammals[11]. *CTNNA1* is the most widely expressed, but is absent from populations of migrating neurons[12], whereas *CTNNA3* is expressed predominantly in the myocardium. We confirmed *CTNNA2* expression in human neural tissue (Supplementary Fig. 2a), and found protein co-expression with the migration markers Dcx and Tuj1 in the murine embryonic day E13.5 brain (Supplementary Fig. 2b). As reported in the mouse, a rim of αN-catenin was expressed in the apically localized progenitors of the ventricular zone[12]. In 20-week-gestation human fetal brain, αN-catenin was mostly restricted to regions expressing DCX and TUJ1 in the developing cortical plate and marginal zone (Supplementary Fig. 2c).

There are two mouse lines harboring loss-of-function mutations of the ortholog to human *CTNNA2* (*Catna2*). *Cerebellar deficient folia* (*cdf*) mice have a spontaneous carboxy (C)-terminal deletion[13–15], and the conventional knockout removed the first exon[16]. These mutants share multiple phenotypes, including impaired lamination of a subset of Purkinje and hippocampal neurons[13–16], hippocampal dendritic spine morphogenesis[16,17], axon projections, positioning of subsets of nuclei-specific neurons, and midline axonal crossing[18]. Of note, many of the phenotypes present in *Catna2* mice are shared with *CTNNA2* patients, including cerebellar hypoplasia and midline defects; however, neither line showed evidence of an overt neocortical phenotype[15]. This was not surprising given that mouse models for human cortical migration defects typically show no neocortical defects.

To investigate migration in a human model, we generated induced pluripotent stem cells (iPSCs) and neuronal derivatives from the affected and unaffected members of family 1263 (1263A and the control, respectively) and an individual with LIS due to Miller–Dieker syndrome (MDS; deletion of chromosome 17p11.3), as well as targeting the *CTNNA2* gene in the H9 human embryonic stem cell (hESC) line (herein referred to as *CTNNA2*^{KO})[19] (Supplementary Fig. 3). Western blot of the neuronal progenitor cells (NPCs) demonstrated absent αN-catenin protein in the patient and knockout compared with the control (Supplementary Fig. 4).

To study migration, we adopted a neurosphere assay[20], and measured neuronal cell body distances from the edge after 48 h. First, we confirmed that cells exiting the neurosphere expressed postmitotic neuronal markers and were negative for other lineages (Supplementary Fig. 5a,b). Glial fibrillary acidic protein–positive cells were only observed at the edge of the plated spheres in all of the lines tested (Supplementary Fig. 5a,b). Cell bodies of control neurons showed a migration front at 514 μm (Fig. 2a; average: 115 μm; s.d.: 97 μm), whereas for MDS (average: 31 μm; s.d.: 22 μm; $P = 3.28 \times 10^{-34}$), *CTNNA2* patients (average: 33 μm; s.d.: 21 μm; $P = 1.19 \times 10^{-27}$), and *CTNNA2*^{KO} lines (average: 36 μm; s.d.: 22 μm; $P = 1.01 \times 10^{-18}$), migration was less than half that of normal cells. Consistent with what has been observed in MDS and control cerebral organoid models of neuronal migration[21], the distribution of distances of MDS, *CTNNA2* patients, and *CTNNA2*^{KO} exited neurons was significantly reduced (Fig. 2a and Supplementary Figs. 6 and 7). We conclude that loss of *CTNNA2* results in a neuronal migration defect in vitro.

Time-lapse phase microscopy was performed to study the mechanism of defective migration. Control cells displayed bipolar morphology, with an average leading neurite length of 130 μm. *CTNNA2*-mutant cells showed shortened (average length: 18 μm) disorganized leading processes, enlarged growth cones, proximal ectopic filopodia and lamellipodia, and failed bipolar morphology (Fig. 2b and Supplementary Videos 1–3). We confirmed that the neurite length and migration defect were due to the absence of *CTNNA2* using lentiviral transduction rescue with green fluorescent protein (GFP)-tagged *CTNNA2*. Transduced cells had uniform expression of a full-length αN-catenin-GFP at 129 kDa and a processed product at 102 kDa (Supplementary Fig. 8a). Neurite length and migration were largely restored in both patient and *CTNNA2*^{KO} cells upon *CTNNA2*-GFP forced expression (Fig. 2b,c and Supplementary Figs. 6 and 7).

Previous studies have shown that mouse αE-catenin, encoded by *Catna1*, is required for preimplantation epithelial integrity[22], whereas conditional deletion in the embryonic brain disrupts adherens junctions, leading to dysregulated proliferation[23]. To test whether loss of *CTNNA2* affects neuroepithelium polarity, we generated neural rosettes from the control and 1263A iPSCs and used immunostaining to examine apical polarization. Despite the absence of αN-catenin at the apical surface of the rosette, the tight junction marker zonula occludens-1 and the adherens junction markers N-cadherin and β-catenin were localized in a polarized fashion near cilia (Supplementary Fig. 9). These results suggest that loss of *CTNNA2* does not adversely affect apical polarization of neuroepithelial cells in culture.

The presence of a putative β-catenin binding domain suggests αN-catenin loss may alter Wnt signaling[24]. We therefore compared gene expression profiles between MDS, 1263A and control NPCs by RNA sequencing. We found no consistent, differential expression changes, arguing against a major transcriptional effect (Supplementary Fig. 10a–c). Furthermore, established canonical Wnt target genes were not changed (Supplementary Fig. 10d), suggesting that the loss of *CTNNA2* does not measurably impact Wnt-mediated transcription.

We thus focused on potential αN-catenin regulation of the neuronal cytoskeleton. αN-catenin contains a putative F-actin-binding domain (ABD) at the C terminus. To assess the ability of αN-catenin to directly bind and bundle actin, we performed actin binding and bundling assays in vitro. Similar to the α-actinin control, full-length recombinant αN-catenin co-sedimented with F-actin (Fig. 3a and Supplementary Fig. 11). Full-length αN-catenin appeared to weakly bundle F-actin filaments (Fig. 3b), although more work is necessary to assess direct bundling activity. There was no noticeable change in the G-actin/F-actin ratio in NPCs from the control or affected patient (Supplementary Fig. 12), arguing against an overall effect on actin stabilization.

Next, we generated lentiviral constructs lacking or containing amino acids 671–905, corresponding to the αN-catenin ABD[25], and confirmed that encoded protein was stable in the NPCs (Supplementary Fig. 8b,c). *CTNNA2*$^{\Delta ABD}$ could not rescue migration defects in the *CTNNA2*^{KO} neurons, and had no effect on control cells (Fig. 3c and Supplementary Figs. 6 and 7). In contrast, expression of *CTNNA2*^{ABD} alone mediated rescue of migration in *CTNNA2*^{KO}, and enhanced migration in control neurons (Fig. 3c and Supplementary Figs. 6 and 7). We conclude that the ABD of *CTNNA2* is necessary and sufficient for its effect on neuronal migration in *CTNNA2*-mutant cells.

The reduction in leading process stability we observed in *CTNNA2*-mutant neurons was similar to a phenotype recently described in mouse *Arpc2*-mutant radial glia[26], suggesting that αN-catenin might regulate Arp2/3 activities. Recombinant α E-catenin controls actin-filament organization and represses Arp2/3-mediated actin polymerization in vitro[25]. Thus, we reasoned

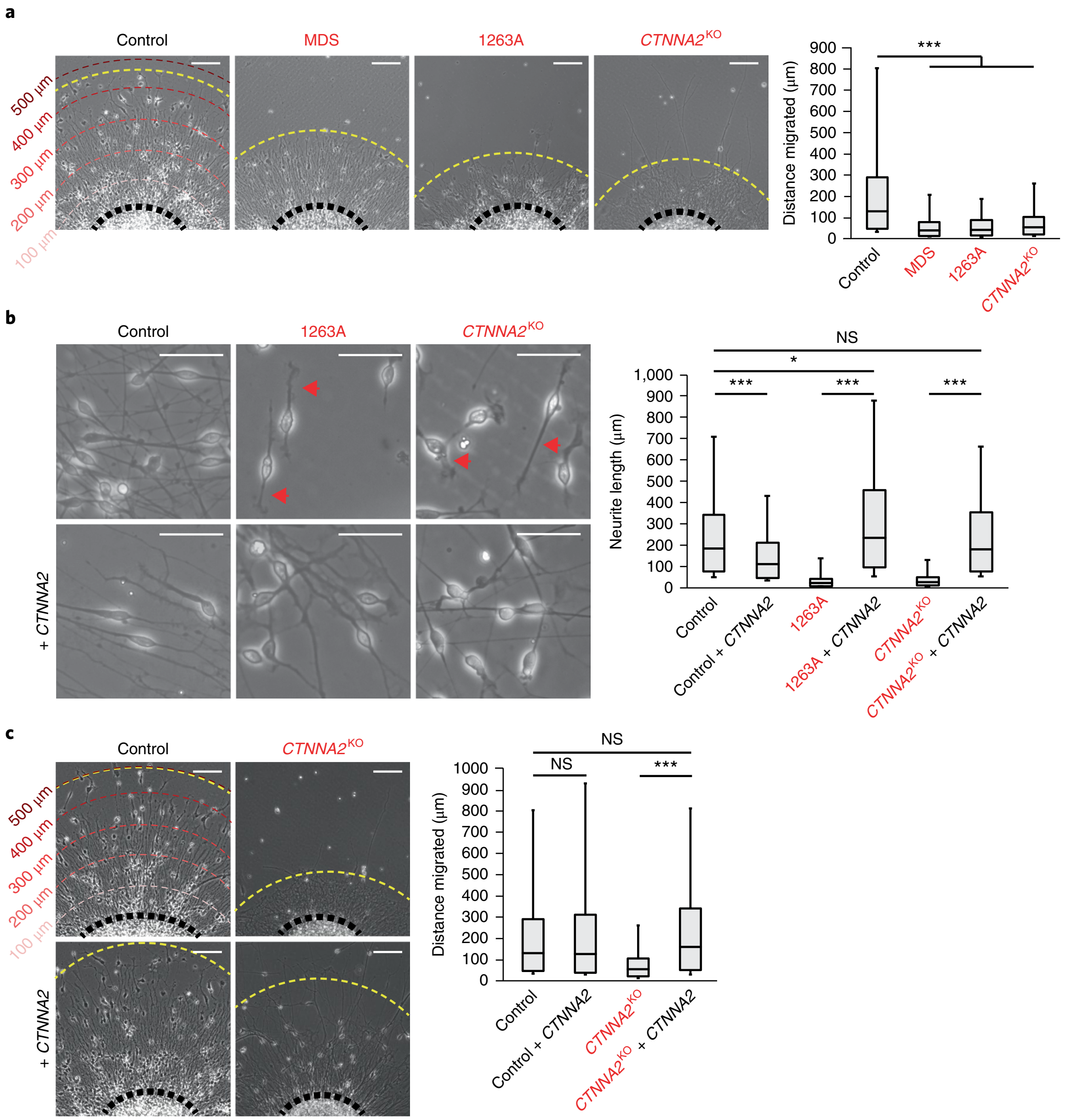

Fig. 2 | Loss of *CTNNA2* mirrors MDS migration phenotypes in iPSC-derived neurons. a, Left: quantification of neuronal migration from human iPSC-derived neurospheres. MDS-derived neurons do not migrate as far as control neurons. Migrating neurons from the affected member of family 1263 (1263A) showed reduced migration similar to *CTNNA2*^{KO} neurons. Scale bars: 100 μm. Right: box plot of the distribution of migrating neurons. Measurements were repeated in three independent iPSC clones per patient, or three *CTNNA2*^{KO} clones ($n = 828$ cells scored). **b**, Left: control neurons show bipolar morphology with long extended primary neurites. *CTNNA2* patient and knockout neurons show thickened, short neurites (red arrows), rescued by forced expression of *CTNNA2*. Scale bars: 50 μm. Right: box plot of the distribution of neurite length. Measurements were repeated in three independent iPSC clones per patient, or three *CTNNA2*^{KO} clones ($n = 552$ cells scored). **c**, Left: rescue of neuronal cell body migration distance upon forced expression of *CTNNA2* in *CTNNA2*^{KO} lines. Scale bars: 100 μm. Right: Box plot of the distribution of migrating neurons. Measurements were repeated in three *CTNNA2*^{KO} clones ($n = 532$ cells scored). In **a**–**c**, box plots show quartile 1 (bottom of box), the median, and quartile 3 (top of box), while the whiskers represent the minimum and maximum values observed in the dataset. $^{*}P < 0.05$; $^{***}P < 0.0001$; NS, not significant.

that the excessive filopodia formation, accompanied by repeated, rapid retraction of the leading process in *CTNNA2*-mutant neurons, might result from failure to suppress ARP2/3-mediated actin branching. To initiate actin branching, the ARP2/3 complex binds to the side of existing F-actin filaments to nucleate a new filament at a distinctive 70° angle; consequently, ARP2 and ARP3 are incorporated into the microfilament structure[27]. To test for increased F-actin branching, we assessed the amount of ARP3 protein associated with F-actin filaments. Migrating neurons from the MDS patient showed ARP3 associated with actin to be equal to or less than in the control, whereas neurons from 1263A and *CTNNA2*^{KO} lines showed almost a 50% increase in association (Fig. 4a,c and Supplementary Fig. 13a,b). We conclude that *CTNNA2*-deficient cells show excessive association between ARP2/3 and actin.

ARP2/3 initiates actin branching in the presence of the WASP VCA (verprolin, cofilin, acidic) domain by the nucleation of F-actin filaments. Therefore, we tested whether αN-catenin was sufficient to inhibit the effect of ARP2/3 + VCA on actin polymerization. The recombinant VCA domain of human WASP (400 nM) showed minimal actin polymerizing activity. This was more than doubled upon

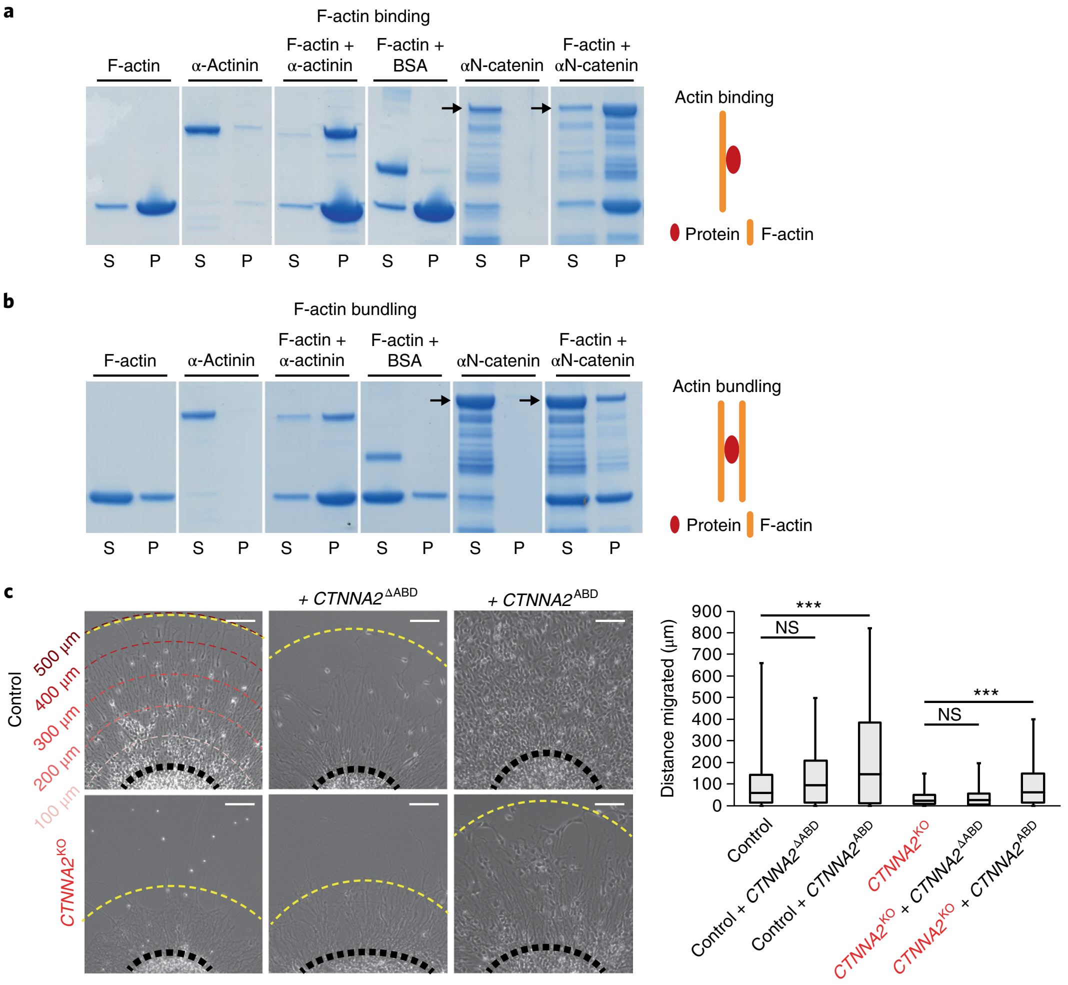

Fig. 3 | Recombinant αN-catenin associates with F-actin, and the actin-binding domain is necessary and sufficient for rescue of neuronal migration. **a**, αN-catenin binds to F-actin in co-sedimentation assays. Most F-actin was present in the pellet (P) upon 100,000*g* spin. While α-actinin was observed primarily in the supernatant (S) when centrifuged alone, when sedimented with F-actin, it shifted to the P. Bovine serum albumin (BSA) was found in the S even when sedimented with F-actin. αN-catenin was exclusively in the S when centrifuged alone, but when sedimented with F-actin the full-length band shifted to the P. Repeated in duplicate. **b**, αN-catenin weakly promotes bundling of F-actin in an assembly assay. Upon centrifugation at 10,000*g*, F-actin was split between the S and P. While α-actinin was exclusively in the S, when co-pelleted with F-actin, it promoted a shift of actin to the P. BSA showed no bundling activity. Similar to α-actinin, αN-catenin was exclusively in the S, but promoted a slight shift of actin to the P. Repeated in duplicate. **c**, Left: migration assay showing rescue of neuronal migration upon forced lentiviral expression of the actin-binding domain of αN-catenin (*CTNNA2*$^{\mathrm{ABD}}$), but not αN-catenin lacking the actin-binding domain (*CTNNA2*$^{\Delta\mathrm{ABD}}$). Scale bars: 100 μm. Right: box plot of distribution of migrating neurons, showing quartile 1 (bottom of box), the median, and quartile 3 (top of box). The whiskers represent the minimum and maximum values observed in the dataset. Measurements were repeated in three *CTNNA2*$^{\mathrm{KO}}$ clones ($n = 834$ cells scored). ***$P < 0.0001$; NS, not significant.

the addition of 10 nM ARP2/3 complex. Increasing concentrations of recombinant αN-catenin resulted in a dosage-dependent inhibition of the ARP2/3 + VCA effect on actin, reduced nearly back to baseline (Fig. 4b). We conclude that αN-catenin is sufficient to suppress the effect of ARP2/3 + VCA on actin polymerization in vitro.

Since αN-catenin repressed ARP2/3 activity in vitro, we next tested whether this activity was mediated by the ABD using *CTNNA2*$^{\mathrm{KO}}$ neurons. We ectopically expressed the αN-catenin ABD and assessed the amount of ARP3 associated with actin by western blot. We observed a near doubling of ARP3 associated with F-actin, whereas expressing the αN-catenin ABD showed potent loss of most ARP3 bound to actin (Fig. 4c and Supplementary Fig. 13b), suggesting that the ABD domain of αN-catenin is sufficient to regulate ARP2/3–actin interaction. We also tested the ability of the recombinant αN-catenin ABD to repress ARP2/3-mediated actin polymerization in vitro. The ABD of αN-catenin was sufficient to repress ARP2/3-mediated actin polymerization in a dosage-dependent manner (Supplementary Fig. 13c), albeit to a lesser extent than full-length αN-catenin.

If αN-catenin mediates its effects on neuronal morphology through suppression of ARP2/3, inhibition of ARP2/3 should at least partially compensate for the loss of αN-catenin in neurons. To test this, we used two different cell-permeable ARP2/3 inhibitors, CK-666 and CK-869 (ref. [28]), which inhibit ARP2/3 at different sites. After generating a dose-response curve, we analyzed neurite length in control, MDS, patient, and *CTNNA2*$^{\mathrm{KO}}$ migrating neurons after 24 h. Most of the control neurons showed long, extended bipolar neurites with an average length >100 μm. Both inhibitors showed a negative effect on neurite length in control neurons, but *CTNNA2*-mutant cells increased neurite length nearly tenfold, restoring the distribution to near control levels (Fig. 4d and Supplementary Figs. 7 and 14). MDS neurons showed neurites with an average length of 18 μm, without improvement upon ARP2/3 inhibitor treatment. We conclude that ARP2/3

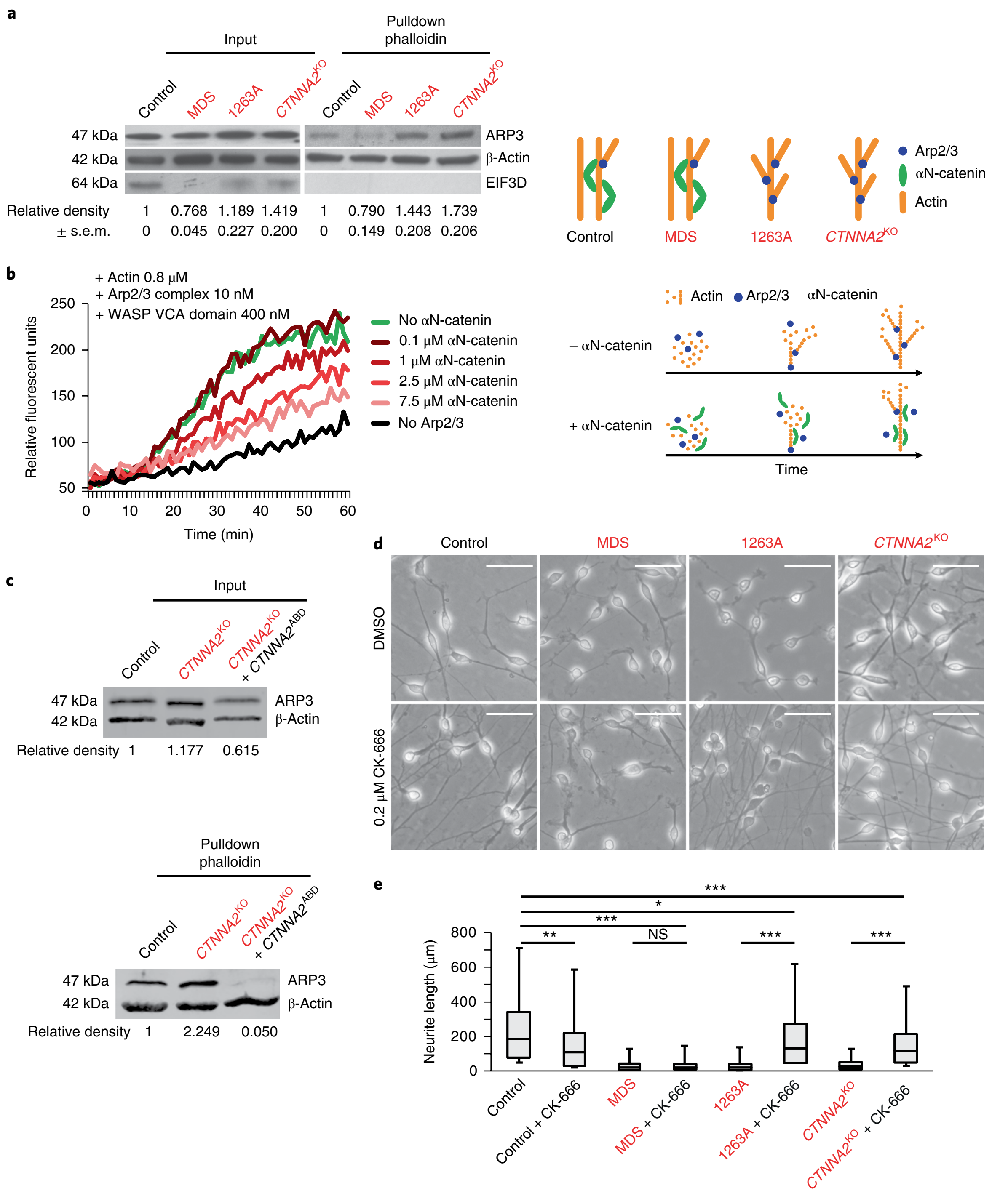

Fig. 4 | αN-catenin represses Arp2/3–actin association and polymerization. **a**, Elevated association between affinity-purified F-actin and ARP2/3 in *CTNNA2*-mutant cells. Left: input (basal expression). Right: F-actin pulldown with phalloidin. There is an exaggerated ARP3 band in the 1263A and knockout lines compared with the MDS and control lines. EIF3D (which does not bind actin) was included as a control for pulldown specificity. Cropped images are shown. Repeated in triplicate. Quantification of the relative density and s.e.m. are shown below. Far right: schematic depicting the model. **b**, Left: actin polymerization assay showing dose-dependent inhibition of Arp2/3 + the VCA domain of WASP-mediated actin polymerization by αN-catenin, measured by relative fluorescent units. In the absence of Arp2/3 (black), there was minimal polymerization, but when Arp2/3 + VCA was added (green), polymerization increased substantially, which was reversed upon dose escalation of αN-catenin. Repeated in triplicate. Right: schematic depicting the model. **c**, Loss of association between F-actin and ARP2/3 in *CTNNA2*^{KO} cells expressing the ABD of αN-catenin. Top: input (basal expression of ARP3 and β-actin). Bottom: F-actin pulldown with phalloidin. There is an exaggerated ARP3 band in the knockout neurons, and loss of ARP3 in the ABD-expressing knockout neurons, compared with band in the control line. Quantification by relative fluorescence of ARP3 to β-actin is shown below. Cropped images are shown. Repeated in duplicate. **d**, ARP2/3 inhibition by CK-666 rescued neurite length defects in *CTNNA2*-mutant neurons, but not control and MDS mutant neurons. Scale bars: 50 μm. **e**, Quantification of **d**, showing quartile 1 (bottom of box), the median, and quartile 3 (top of box). Whiskers represent the minimum and maximum values observed in the dataset. Measurements were repeated in three independent iPSC clones per patient, or three *CTNNA2*^{KO} clones ($n = 442$ cells scored). *$P < 0.05$; **$P < 0.001$; ***$P < 0.0001$; NS, not significant.

inhibitors can largely rescue the neurite length defect associated with loss of *CTNNA2*.

In summary, we have identified a new neuronal migration disorder due to biallelic truncating mutations in *CTNNA2*. The involvement of an actin regulator in pachygyria was surprising, given that previous genetic studies focused on microtubules[29]. Microtubules scaffold the cytoskeleton for the repeated cycles of migration[30,31]. The main effect of actin appears to be in sensing and responding to extracellular guidance cues through changes in cell morphology, as well as guiding microtubules within the primary neurite[32]. This is mediated at least in part by calcium influx and enhanced neuronal motility through LIS1-dependent regulation of Rho GTPases[33], but also through transmembrane proteins, which can alter the cell morphology through effects on actin[34].

Actin structure is critically regulated by Arp2/3, which controls the decision to initiate branching. We show that Arp2/3 overactivity, as a result of loss of αN-catenin, leads to excessive branching, which impairs neurite growth and stability, possibly by controlling microtubule advance into the growth cone[32,35]. αN-catenin suppresses actin branching; in vivo, this probably occurs by binding F-actin. This activity is mediated by the ABD, which we show competes with ARP2/3 for nucleation sites on F-actin. α-Actinin, fascin and αE-catenin can sort actin-associated proteins by altering the conformation of actin[1,25,36]. It will be interesting to determine whether αN-catenin also shares this property or whether it extends to other ABD-containing proteins. Thus, as a more general principle, actin-binding proteins may serve unrecognized roles in actin regulation by controlling F-actin polymerization as well as dictating actin conformation locally within a cell.

URLs

NHLBI Exome Sequencing Project (ESP), http://evs.gs.washington.edu/EVS/; SeattleSeq, http://snp.gs.washington.edu/SeattleSeqAnnotation137/; OMIM, http://www.omim.org/; PolyPhen-2, http://genetics.bwh.harvard.edu/pph2/; NCBI Gene *CTNNA2*, https://www.ncbi.nlm.nih.gov/gene/1496; TopHat2, http://ccb.jhu.edu/software/tophat/

Methods

Methods, including statements of data availability and any associated accession codes and references, are available at https://doi.org/10.1038/s41588-018-0166-0.

Received: 19 August 2017; Accepted: 22 May 2018;
Published online: 16 July 2018

References

1. Drees, F., Pokutta, S., Yamada, S., Nelson, W. J. & Weis, W. I. α-Catenin is a molecular switch that binds E-cadherin-β-catenin and regulates actin-filament assembly. *Cell* **123**, 903–915 (2005).
2. Leventer, R. J., Guerrini, R. & Dobyns, W. B. Malformations of cortical development and epilepsy. *Dialogues Clin. Neurosci.* **10**, 47–62 (2008).
3. Ayala, R., Shu, T. & Tsai, L.-H. Trekking across the brain: the journey of neuronal migration. *Cell* **128**, 29–43 (2007).
4. Meyer, G. & Feldman, E. L. Signaling mechanisms that regulate actin-based motility processes in the nervous system. *J. Neurochem.* **83**, 490–503 (2002).
5. Luo, L. Actin cytoskeleton regulation in neuronal morphogenesis and structural plasticity. *Annu. Rev. Cell Dev. Biol.* **18**, 601–635 (2002).
6. Rocca, D. L., Martin, S. P., Jenkins, E. L. & Hanley, J. G. Inhibition of Arp2/3-mediated actin polymerization by PICK1 regulates neuronal morphology and AMPA receptor endocytosis. *Nat. Cell Biol.* **10**, 259–271 (2008).
7. Choi, M. et al. Genetic diagnosis by whole exome capture and massively parallel DNA sequencing. *Proc. Natl. Acad. Sci. USA* **106**, 19096–19101 (2009).
8. DePristo, M. A. et al. A framework for variation discovery and genotyping using next-generation DNA sequencing data. *Nat. Genet.* **43**, 491–498 (2011).
9. Magi, A. et al. H3M2: detection of runs of homozygosity from whole-exome sequencing data. *Bioinformatics* **30**, 2852–2859 (2014).
10. Seelow, D., Schuelke, M., Hildebrandt, F. & Nurnberg, P. HomozygosityMapper—an interactive approach to homozygosity mapping. *Nucleic Acids Res.* **37**, W593–W599 (2009).
11. Ajioka, I. & Nakajima, K. Switching of alpha-catenin from alphaE-catenin in the cortical ventricular zone to alphaN-catenin II in the intermediate zone. *Brain Res. Dev. Brain Res.* **160**, 106–111 (2005).
12. Stocker, A. M. & Chenn, A. Differential expression of alpha-E-catenin and alpha-N-catenin in the developing cerebral cortex. *Brain Res.* **1073–1074**, 151–158 (2006).
13. Park, C., Falls, W., Finger, J. H., Longo-Guess, C. M. & Ackerman, S. L. Deletion in Catna2, encoding αN-catenin, causes cerebellar and hippocampal lamination defects and impaired startle modulation. *Nat. Genet.* **31**, 279–284 (2002).
14. Park, C., Longo, C. M. & Ackerman, S. L. Genetic and physical mapping of the cerebellar deficient folia (cdf) locus on mouse chromosome 6. *Genomics* **69**, 135–138 (2000).
15. Park, C., Finger, J. H., Cooper, J. A. & Ackerman, S. L. The cerebellar deficient folia (*cdf*) gene acts intrinsically in Purkinje cell migrations. *Genesis* **32**, 32–41 (2002).
16. Togashi, H. et al. Cadherin regulates dendritic spine morphogenesis. *Neuron* **35**, 77–89 (2002).
17. Abe, K., Chisaka, O., van Roy, F. & Takeichi, M. Stability of dendritic spines and synaptic contacts is controlled by alpha N-catenin. *Nat. Neurosci.* **7**, 357–363 (2004).
18. Uemura, M. & Takeichi, M. αN-catenin deficiency causes defects in axon migration and nuclear organization in restricted regions of the mouse brain. *Dev. Dyn.* **235**, 2559–2566 (2006).
19. Chambers, S. M. et al. Highly efficient neural conversion of human ES and iPS cells by dual inhibition of SMAD signaling. *Nat. Biotechnol.* **27**, 275–280 (2009).
20. Katakowski, M., Zhang, Z., deCarvalho, A. C. & Chopp, M. EphB2 induces proliferation and promotes a neuronal fate in adult subventricular neural precursor cells. *Neurosci. Lett.* **385**, 204–209 (2005).
21. Bershteyn, M. et al. Human iPSC-derived cerebral organoids model cellular features of lissencephaly and reveal prolonged mitosis of outer radial glia. *Cell Stem Cell* **20**, 435–449.e4 (2017).
22. Torres, M. et al. An *α-E-catenin* gene trap mutation defines its function in preimplantation development. *Proc. Natl. Acad. Sci. USA* **94**, 901–906 (1997).
23. Lein, W.-H., Klezovitch, O., Fernandez, T. E., Delrow, J. & Vasioukhin, V. αE-catenin controls cerebral cortical size by regulating the hedgehog signaling pathway. *Science* **311**, 1609–1612 (2006).
24. Pokutta, S. & Weis, W. I. Structure of the dimerization and β-catenin-binding region of α-catenin. *Mol. Cell* **5**, 533–543 (2000).
25. Hansen, S. D. et al. αE-catenin actin-binding domain alters actin filament conformation and regulates binding of nucleation and disassembly factors. *Mol. Biol. Cell* **24**, 3710–3720 (2013).
26. Wang, P.-S. et al. Crucial roles of the Arp2/3 complex during mammalian corticogenesis. *Development* **143**, 2741–2752 (2016).
27. Rouiller, I. et al. The structural basis of actin filament branching by the Arp2/3 complex. *J. Cell Biol.* **180**, 887–895 (2008).
28. Hetrick, B., Han, M. S., Helgeson, L. A. & Nolen, B. J. Small molecules CK-666 and CK-869 inhibit actin-related protein 2/3 complex by blocking an activating conformational change. *Chem. Biol.* **20**, 701–712 (2013).
29. Wynshaw-Boris, A., Pramparo, T., Youn, Y. H. & Hirotsune, S. Lissencephaly: mechanistic insights from animal models and potential therapeutic strategies. *Semin. Cell Dev. Biol.* **21**, 823–830 (2010).
30. Moon, H. M. & Wynshaw-Boris, A. Cytoskeleton in action: lissencephaly, a neuronal migration disorder. *Wiley Interdiscip. Rev. Dev. Biol.* **2**, 229–245 (2013).
31. Solecki, D. J., Model, L., Gaetz, J., Kapoor, T. M. & Hatten, M. E. Par6α signaling controls glial-guided neuronal migration. *Nat. Neurosci.* **7**, 1195–1203 (2004).
32. Strasser, G. A., Rahim, N. A., VanderWaal, K. E., Gertler, F. B. & Lanier, L. M. Arp2/3 is a negative regulator of growth cone translocation. *Neuron* **43**, 81–94 (2004).
33. Kholmanskikh, S. S., Dobrin, J. S., Wynshaw-Boris, A., Letourneau, P. C. & Ross, E. M. Disregulated RhoGTPases and actin cytoskeleton contribute to the migration defect in Lis1-deficient neurons. *J. Neurosci.* **23**, 8673–8681 (2003).
34. Chai, X., Forster, E., Zhao, S., Bock, H. H. & Frotscher, M. Reelin stabilizes the actin cytoskeleton of neuronal processes by inducing n-cofilin phosphorylation at serine3. *J. Neurosci.* **29**, 288–299 (2009).
35. Zhou, F.-Q., Waterman-Storer, C. M. & Cohan, C. S. Focal loss of actin bundles causes microtubule redistribution and growth cone turning. *J. Cell Biol.* **157**, 839–849 (2002).
36. Winkelman, J. D. et al. Fascin- and α-actinin-bundled networks contain intrinsic structural features that drive protein sorting. *Curr. Biol.* **26**, 2697–2706 (2016).

Acknowledgements

We thank the patients and their families for participation. We thank A. Wynshaw-Boris for generous scientific and editorial input. The research was supported by NIH R01NS041537, R01NS048453, R01NS052455, P01HD070494, P30NS047101, Qatar National Research Fund number 6-1463-351, the Simons Foundation Autism Research Initiative, and the Howard Hughes Medical Institute (to J.G.G). A.E.S. is a recipient of an A.P. Giannini Fellowship and an NIH Pathway to Independence Award, R00HD082337. S.T.B. is supported by a 2014 NARSAD Young Investigator Grant from the Brain and Behavior Research Foundation. We thank the Broad Institute and Yale Center for Mendelian Disorders (UMIHG008900 to D. MacArthur and H. Rehm, and UMIHG006504 to R. Lifton and M.G.), and the Gregory M. Kiez and Mehmet Kutman Foundation (to M.G). We acknowledge M. Gerstein, S. Mane, A. B. Ekici, and S. Uebe for sequencing support and analysis, the Yale Biomedical High Performance Computing Center for data analysis and storage, the Yale Program on Neurogenetics, and the Yale Center for Human Genetics and Genomics. Exome data have been deposited into the database of Genotypes and Phenotypes (phs000288).

Author contributions

N.A-S., H.Y.A-A., H.Kaymakçalan, C.Y., R.O.R., V.S., K.N.J., M.S.Z., S.E., T.B-O., A.Karminejad, H.Kayserili, F.M., M.K., E.Fenercioglu, B.K., H.M., F.I., S.D., Y.A., E.Faqeih, G.M., B.A.B., L.M., I.M., B.S., J.C., W.B.D., M.G., J.G.G., and R.A.J. performed the patient recruitment and phenotyping. A.E.S., A.O.C., S.T.B., B.C., D.M., E.C.S., K.B., J.L.S., M.G., and J.G.G. supported the sequencing and variant interpretation. A.E.S., N.C., R.W., and R.N. performed the tissue culture experiments. A.E.S. and A.Kalur generated recombinant proteins and performed the actin assays. A.E.S., M.W.B., and J.G.G. wrote and edited the manuscript. J.G.G. directed the project.

Competing interests

The authors declare no competing interests.

Additional information

Supplementary information is available for this paper at https://doi.org/10.1038/s41588-018-0166-0.

Reprints and permissions information is available at www.nature.com/reprints.

Correspondence and requests for materials should be addressed to A.E.S. or J.G.G.

Publisher's note: Springer Nature remains neutral with regard to jurisdictional claims in published maps and institutional affiliations.

Methods

Patient recruitment. Patients were enrolled and sampled according to protocols for standard local practice in approved human subjects at the respective institutions. Each subject was evaluated, and had MRI images taken, by one of the authors. We excluded cases with overlapping conditions such as asymmetrical brain dysplasia, primary white matter disease, or evidence of altered metabolism, such as elevations in lactate or abnormal peaks on standard clinical serum tandem mass spectroscopy.

Exome sequencing. For each sample, DNA was extracted from peripheral blood leukocytes by salt extraction. Exon capture was performed with the Agilent SureSelect Human All Exome 50 Mb Kit with paired-end sequencing on an Illumina HiSeq 2000 instrument, resulting in >94% recovery at >10× coverage.

Sequences were aligned to the human genome (hg19) with the Burrows–Wheeler Aligner, and variants were delineated using the Genome Analysis Toolkit software and SAMtools algorithms for both SNPs and insertion and deletion polymorphisms[8]. Variants were filtered for the criteria: (1) occurring in coding regions and/or splice sites; (2) non-synonymous; (3) found in less than 0.1% frequency in control populations (our in-house exome dataset of 12,000 individuals, Single Nucleotide Polymorphism database (dbSNP) and Exome Variant Server); (4) homozygous in consanguineous families; and (5) within linkage intervals or blocks of homozygosity. Variants were ranked by the type of mutation (nonsense/splice/indel > missense), amino acid conservation across species, and damage prediction programs (PolyPhen and Grantham score).

Linkage analysis. All informative members of family 1101 were genotyped with the Infinium iSelect24 mapping panel (Center for Inherited Disease Research) and analyzed with easyLINKAGE-Plus software[37]. Parameters were autosomal recessive with full penetrance and a disease allele frequency of 0.001. Genomic regions with logarithm of the odds scores below −2 were excluded as loci, those above 2 were considered as candidate loci, and those above 3.3 were considered as statistical evidence for genome-wide significance. Linkage simulations were performed with Allegro 1.2c under the same parameters, with 5,000 markers at average intervals of 0.64 cM, co-dominant allele frequencies, and parametric calculations[37].

Tissue culture. Fibroblasts were generated from unaffected and affected dermal biopsy explants and cultured in Minimum Essential Media (Gibco), supplemented with 20% fetal bovine serum (Gemini). iPSCs, neural progenitor cells, and neurons were obtained as previously described[19,38]. MDS fibroblasts were obtained from the Coriell BioRepository (GM09209) and similarly reprogrammed.

iPSCs were generated as previously described[39] using 3 μg expression plasmid mixtures (OCT3/4, SOX2, KLF4, L-MYC, LIN28, and p53 shRNA) electroporated into 6×10^5 cells. These were dissociated after 7 d, and 1.5×10^5 cells were re-plated onto 100 mm dishes with 1.5×10^5 irradiated CF-1 mouse embryonic fibroblasts as a feeder layer. Culture medium was replaced every day with hESC/iPSC medium (Dulbecco's modified Eagle medium/nutrient mixture F-12 (DMEM/F12) supplemented with 20% knockout serum replacement and 20 ng ml^{-1} bFGF (Invitrogen), 1× non-essential amino acids, and 110 mM 2-mercaptoethanol). Colonies with healthy appearance (rounded smooth edges) were selected for further cultivation and evaluation. After three passages, iPSCs were transferred to Matrigel (BD Biosciences)-coated plates and grown in mTeSR medium (Stemcell Technologies).

NPCs were obtained as previously described[40] with embryoid bodies formed by mechanical dissociation of cell clusters and plated in suspension in differentiation medium (DMEM/F12, 1× N2, 1 μM Dorsomorphin (Tocris Bioscience), and 2 μM A8301 (Tocris Bioscience)) and shaken constantly at 95 r.p.m. for 7 d, then plated onto Matrigel (BD Biosciences)-coated dishes in NPC medium (DMEM/F12, 0.5× N2, 0.5× B27, and 20 ng ml^{-1} bFGF). Rosettes were visible after 5–7 d. They were selected with Neural Rosette Selection Reagent (Stemcell Technologies), and were NPCs plated onto poly-L-ornithine/laminin (Sigma) dishes with NPC medium, which was exchanged every 2 d.

Bright-field images were taken on Axio Vert.A1 or Axio Observer inverted microscopes (Zeiss), in addition to an EVOS microscope (Life Technologies), and processed using Photoshop CS5 (Adobe Systems). Time-lapse videos were acquired on a Zeiss Axio Observer and compiled with Zeiss ZEN software. Fluorescent confocal images of neural rosettes were taken on an LSM 880 (Zeiss) and processed using Fiji/ImageJ software. Images are maximum z projections of the entire depth of signal for the cell of interest.

CRISPR targeting. Frame-shifting insertions or deletions (indels), occurring in coding exon 12 of *CTNNA2*, were generated in H9 hESCs by CRISPR–SpCas9-induced imprecise non-homologous end joining as previously described[41] with CTNNA2 sgRNA-F and CTNNA2 sgRNA-R primers (Supplementary Table 1) into BbsI-digested px330. Individual colonies were isolated after two weeks, expanded, and genotyped by Sanger sequencing for biallelic mutations.

Complementary DNA synthesis and RT-PCR. Complementary DNA (cDNA) synthesis of 1 μg patient RNA was performed using Superscript III First-Strand PCR with reverse transcription (RT-PCR) (Life Technologies). The reaction products were then used for quantitative real-time PCR (qRT-PCR) or cloning. qRT-PCR was performed in triplicate on 10 ng human cDNA for *CTNNA2*, *AXIN2*, *ID2*, *LEF1*, and *GAPDH* (see Supplementary Table 1 for primer sequences). Values were normalized to *GAPDH* as a loading control and the fold-change was calculated in reference.

Neurosphere assays. Neurosphere assay methods were modified from previously described protocols[42]. Three different stem cell lines (clones) per patient or condition were used as biological replicates for each experiment. The iPSC-derived NPCs were dissociated and incubated, shaking at 95 r.p.m, in NPC media. The following day, the media was changed to DMEM/F12 with 1× N2 and 1× B27, and shaking at 95 r.p.m for 12 h. The resultant neurospheres were plated on poly-L-ornithine/laminin plates, and imaged at 48 h to record the distance each neuronal cell body traveled from the edge of the neurosphere using Fiji/ImageJ (National Institutes of Health (NIH)) per clone. Data from each clone were collected and analyzed together with data from the other two clones per patient or condition to facilitate the statistical tests.

Neurite quantification. Three different stem cell lines (clones) per patient or condition were used as biological replicates for each experiment. To assess the leading process length, stem-cell-derived migrating neurons were imaged. The length of the primary neurite from the edge of the cell body to the tip of the growth cone was measured in micrometres. For ARP2/3 inhibition, 0.2 μM CK-666, 0.2 μ M CK-869, or an equivalent dilution of DMSO was added to the neurons 6 h after plating[28]. Neurons were analyzed after 24 h. Data from each clone were collected and analyzed together with data from the other two clones per patient or condition to facilitate the statistical tests.

RNA sequencing. Total RNA was extracted from two NPC lines per patient with TRIzol Reagent (Gibco). Full-length messenger RNA was captured using a TruSeq Stranded mRNA kit (Illumina) with the standard protocol, and submitted for paired-end 100-nucleotide sequencing on MiSeq (Illumina). Roughly 30 million reads per sample were aligned to the 1000 Genomes Project's version of GRCh37 using standard TopHat2 (see URLs) v2.0.11 with paired-end read options and allowing for intron-spanning reads as defined by transcripts in Illumina iGenomes NCBI build 37.2. The pairwise Euclidean distance between all samples using the filtered (median fragments per kilobase of transcript per million mapped reads > 1) and $\log_2$-transformed gene expression values was calculated, and the Pearson's correlation was determined. Differential expression on a gene-based level was tested for with cuffdiff 59 v2.1.1 using the default option. Genes reported as significantly differentially expressed between a pair of conditions were determined based on a cuffdiff threshold of a false-discovery-rate-corrected P value of 0.05.

Histology. Animal use followed NIH guidelines and was approved by the Institutional Animal Care and Use Committee at the University of California, San Diego and Rockefeller University. Wild-type mice (C57BL/6N) were obtained from Jax and intercrossed to produce embryonic day E13.5 embryos. The embryos were fixed in 4% paraformaldehyde (PFA), cryoprotected, then sectioned. Human fetal brain was obtained from the University of California, San Diego autopsy service, fixed in 4% PFA and embedded in paraffin. Microtome sections were deparaffinized, blocked with 4% donkey serum, incubated in primary antibody overnight, washed, incubated in secondary antibody for 1 h, post-fixed in 4% PFA, and counterstained with 4′,6-diamidino-2-phenylindole or Nissl for imaging.

αN-catenin lentivirus. Full-length, the ABD (amino acids 671–905) or ABD-deleted (ΔABD; amino acids 1–670) αN-catenin was cloned into pLVX-AcGFP-N1 vector (Clontech) and co-transfected with psPAX2 and pCMV-VSVg (Addgene) into Lenti-X 293T cells (Clontech) to generate lentivirus. Virus-containing media was collected at 66 h, concentrated by ultracentrifuge, and stored at −80 °C. Patient-derived NPCs were transduced with lentivirus and selected with 1 μg ml^{-1} puromycin for 48 h before proceeding with the experiments.

Recombinant αN-catenin protein generation. cDNA encoding full-length αN-catenin was amplified and cloned into bacterial glutathione-S-transferase (GST) expression vector pGEX-6P-1 (GE Healthcare Life Sciences). Recombinant αN-catenin was produced in BL21 cells and affinity purified with anti-GST MagneGST beads (Promega).

Actin assays. Actin binding and bundling assays were performed according to the manufacturer's recommendations (BK001; Cytoskeleton). Actin polymerization assays were performed with pyrene actin (AP05; Cytoskeleton), α-actinin, the GST-tagged VCA domain of human WASP protein (#VCG03), and Arp2/3 protein complex from porcine brain (RP01P; Cytoskeleton) according to the manufacturer's recommendations, with the addition of recombinant αN-catenin. G-Actin/F-Actin ratios were determined in triplicate from patient-derived NPCs using the G-Actin/F-Actin In Vivo Assay Biochem Kit (BK037; Cytoskeleton). CK-666 and CK-869 block an activating conformational change, binding to different sites[28]. CK-666 stabilizes the inactive state of the complex, blocking movement of the Arp2 and Arp3 subunits into the activated filament-like (short pitch) conformation, while CK-869 binds to a serendipitous pocket on Arp3 and allosterically destabilizes the short-pitch Arp3–Arp2 interface.

F-actin pulldown. Phalloidin-mediated F-actin pulldown was performed as described[43] with Biotin-XX Phalloidin (B7474; Life Technologies) then streptavidin conjugated magnetic beads (Pierce Protein Biology), washed 3×, then boiled.

Antibodies. Primary antibodies used for immunocytochemistry or western blot include mouse anti-GAPDH (Millipore), mouse anti-Nestin (Millipore), mouse anti-Tuj1/βIII-tubulin (Millipore), mouse anti-Tuj1/βIII-tubulin (Santa Cruz Biotechnology), mouse anti-TRA-1-60 (Millipore), mouse anti-TRA-1-81 (Millipore), goat anti-Lin28a (R&D Systems), rabbit anti-Nanog (Santa Cruz Biotechnology), rabbit anti-Oct3/4 (Santa Cruz Biotechnology), rabbit anti-DCX[44], goat anti-DCX (Santa Cruz Biotechnology), goat anti-SOX2 (Santa Cruz Biotechnology), rabbit anti-PAX6 (Covance), mouse anti-MAP2 (Millipore), mouse anti-BLBP (Abcam), rabbit anti-GFAP (Sigma), rabbit anti-OLIG2 (Abcam), mouse anti-β-Catenin (BD Biosciences), rabbit anti-Arp3 (Santa Cruz Biotechnology), mouse anti-β-actin (Sigma), rabbit anti-EIF3D (Bethyl Laboratoriess), rat anti-αN-catenin obtained from the NIH Eunice Kennedy Shriver National Institute of Child Health and Human Development Developmental Studies Hybridoma Bank (Catalog: NCAT2, deposited by M. Takeichi and S. Hirano). Fluorophore conjugated secondary antibodies were purchased from Invitrogen, and immunohistochemistry was performed with an ABC Elite Peroxidase Staining Kit, using ImmpactDAB as a substrate.

Statistics. Neuronal migration and neurite length were graphed in Microsoft Excel as a box plot with quartile 1, the median, and quartile 3 displayed. Whiskers represent the maximum and minimum observed values for each comparison group across all replicates. Western blot densitometry and fold-change gene expression were plotted as a bar graph with the average of at least three replicates displayed, or the values displayed on the figure. Error bars represent the s.e. of the mean. Unpaired, two-tailed Student's *t*-tests were used to calculate significance ($*P<0.05$; $**P<0.001$; $***P<0.0001$; NS, not significant). Figure 2a: control versus MDS, $P=3.29\times10^{-34}$; control versus 1263A, $P=1.20\times10^{-27}$; control versus *CTNNA2*$^{\mathrm{KO}}$, $P=1.01\times10^{-18}$. Figure 2b: control versus 1263A, $P=2.74\times10^{-26}$; control versus *CTNNA2*$^{\mathrm{KO}}$, $P=4.03\times10^{-57}$; control versus control + *CTNNA-GFP*, $P=2.64\times10^{-7}$; 1263A versus 1263A + *CTNNA-GFP*, $P=4.30\times10^{-26}$; *CTNNA2*$^{\mathrm{KO}}$ versus *CTNNA2*$^{\mathrm{KO}}$ + *CTNNA-GFP*, $P=1.66\times10^{-59}$; control versus 1263A + *CTNNA-GFP*, $P=0.04$; control versus *CTNNA2*$^{\mathrm{KO}}$ + *CTNNA-GFP*, $P=0.73$. Figure 3c: control versus control + *CTNNA-GFP*, $P=0.29$; *CTNNA2*$^{\mathrm{KO}}$ versus *CTNNA2*$^{\mathrm{KO}}$ + *CTNNA-GFP*, $P=1.15\times10^{-21}$; control versus *CTNNA2*$^{\mathrm{KO}}$ + *CTNNA-GFP*, $P=0.10$. Figure 3c: control versus control + *CTNNA*$^{\Delta\mathrm{ABD}}$, $P=0.65$; control versus control + *CTNNA*$^{\mathrm{ABD}}$, $P=2.68\times10^{-21}$; *CTNNA2*$^{\mathrm{KO}}$ versus *CTNNA2*$^{\mathrm{KO}}$ + *CTNNA*$^{\Delta\mathrm{ABD}}$, $P=0.06$; *CTNNA2*$^{\mathrm{KO}}$ versus *CTNNA2*$^{\mathrm{KO}}$ + *CTNNA*$^{\mathrm{ABD}}$, $P=1.81\times10^{-30}$. Figure 4c: control versus control + CK-666, $P=3.37\times10^{-3}$; MDS versus MDS + CK-666, $P=0.29$; 1263A versus 1263A + CK-666, $P=5.75\times10^{-19}$; *CTNNA2*$^{\mathrm{KO}}$ versus *CTNNA2*$^{\mathrm{KO}}$ + CK-666, $P=3.48\times10^{-52}$; control versus MDS + CK-666, $P=2.12\times10^{-53}$; control versus 1263A + CK-666, $P=0.03$; control versus *CTNNA2*$^{\mathrm{KO}}$ + CK-666, $P=4.86\times10^{-10}$. Supplementary Fig. 4: control versus 1263A, $P=0.003$; no detectable protein in *CTNNA2*$^{\mathrm{KO}}$. Supplementary Fig. 8: *AXIN2* control versus 1263A, $P=0.81$; *ID2* control versus 1263A, $P=0.53$; *LEF1* control versus 1263A, $P=0.32$. Supplementary Fig. 10: control versus 1263A, $P=0.35$. Supplementary Fig. 11: control versus control + CK-869, $P=1.88\times10^{-17}$; MDS versus MDS + CK-869, $P=2.47\times10^{-5}$; 1263A versus 1263A + CK-869, $P=1.18\times10^{-38}$; *CTNNA2*$^{\mathrm{KO}}$ versus *CTNNA2*$^{\mathrm{KO}}$ + CK-869, $P=5.47\times10^{-57}$; control versus MDS + CK-869, $P=1.47\times10^{-61}$; control versus 1263A + CK-869, $P=5.22\times10^{-6}$; control versus *CTNNA2*$^{\mathrm{KO}}$ + CK-666, $P=0.26$.

Reporting Summary. Further information on experimental design is available in the Nature Research Reporting Summary linked to this article.

Data availability. The datasets generated and analyzed for the current study have been deposited in the database of Genotypes and Phenotypes under accessions phs000288 and phs000744, and the Gene Expression Omnibus under accession GSE72994.

References

37. Hoffmann, K. & Lindner, T. H. easyLINKAGE-Plus—automated linkage analyses using large-scale SNP data. *Bioinformatics* **21**, 3565–3567 (2005).
38. Lardelli, R. M. et al. Bi-allelic mutations in the 3′ exonuclease TOE1 cause pontocerebellar hypoplasia and uncover a role in snRNA processing. *Nat. Genet.* **49**, 457–464 (2017).
39. Okita, K. et al. A more efficient method to generate integration-free human iPS cells. *Nat. Methods* **8**, 409–412 (2011).
40. Marchetto, M. C. N. et al. A model for neural development and treatment of Rett syndrome using human induced pluripotent stem cells. *Cell* **143**, 527–539 (2010).
41. Ran, F. A. et al. Genome engineering using the CRISPR–Cas9 system. *Nat. Protoc.* **8**, 2281–2308 (2013).
42. Youn, Y. H., Pramparo, T., Hirotsune, S. & Wynshaw-Boris, A. Distinct dose-dependent cortical neuronal migration and neurite extension defects in *Lis1* and *Ndel1* mutant mice. *J. Neurosci.* **29**, 15520–15530 (2009).
43. Yeung, Y. G., Wang, Y., Einstein, D. B., Lee, P. S. & Stanley, E. R. Colony-stimulating factor-1 stimulates the formation of multimeric cytosolic complexes of signaling proteins and cytoskeletal components in macrophages. *J. Biol. Chem.* **273**, 17128–17137 (1998).
44. Gleeson, J. G., Lin, P. T., Flanagan, L. A. & Walsh, C. A. Doublecortin is a microtubule-associated protein and is expressed widely by migrating neurons. *Neuron* **23**, 257–271 (1999).

nature research

Corresponding author(s): Gleeson, Joseph G

☐ Initial submission ☐ Revised version ☒ Final submission

Life Sciences Reporting Summary

Nature Research wishes to improve the reproducibility of the work that we publish. This form is intended for publication with all accepted life science papers and provides structure for consistency and transparency in reporting. Every life science submission will use this form; some list items might not apply to an individual manuscript, but all fields must be completed for clarity.

For further information on the points included in this form, see Reporting Life Sciences Research. For further information on Nature Research policies, including our data availability policy, see Authors & Referees and the Editorial Policy Checklist.

▸ Experimental design

1. Sample size

Describe how sample size was determined.	LOD scores were estimated using Allegro experiments were run with biological replicates in triplicate.

2. Data exclusions

Describe any data exclusions.	No data was excluded. No other families from our cohort had rare (<0.1% AF) predicted deleterious variants in CTNNA2.

3. Replication

Describe whether the experimental findings were reliably reproduced.	Fig. 2a-c, 3c, 4a-b, d was performed in triplicate, Fig. 3a-b, Fig. 4c was performed in duplicate. Representative images are shown. Suppl Fig 10a-c and Suppl Fig. 13 was performed in duplicate. All other Suppl Figs were performed in triplicate, showing representative data.

4. Randomization

Describe how samples/organisms/participants were allocated into experimental groups.	No randomization was performed.

5. Blinding

Describe whether the investigators were blinded to group allocation during data collection and/or analysis.	Data collection and analysis was not performed blinded.

Note: all studies involving animals and/or human research participants must disclose whether blinding and randomization were used.

6. Statistical parameters

For all figures and tables that use statistical methods, confirm that the following items are present in relevant figure legends (or in the Methods section if additional space is needed).

n/a	Confirmed	
☐	☒	The exact sample size (*n*) for each experimental group/condition, given as a discrete number and unit of measurement (animals, litters, cultures, etc.)
☐	☒	A description of how samples were collected, noting whether measurements were taken from distinct samples or whether the same sample was measured repeatedly
☐	☒	A statement indicating how many times each experiment was replicated
☐	☒	The statistical test(s) used and whether they are one- or two-sided (note: only common tests should be described solely by name; more complex techniques should be described in the Methods section)
☐	☒	A description of any assumptions or corrections, such as an adjustment for multiple comparisons
☐	☒	The test results (e.g. *P* values) given as exact values whenever possible and with confidence intervals noted
☐	☒	A clear description of statistics including central tendency (e.g. median, mean) and variation (e.g. standard deviation, interquartile range)
☐	☒	Clearly defined error bars

See the web collection on statistics for biologists for further resources and guidance.

Software

Policy information about availability of computer code

7. Software

Describe the software used to analyze the data in this study.	EasyLinkage (running Allegro), Excel (statistical analysis)

For manuscripts utilizing custom algorithms or software that are central to the paper but not yet described in the published literature, software must be made available to editors and reviewers upon request. We strongly encourage code deposition in a community repository (e.g. GitHub). *Nature Methods* guidance for providing algorithms and software for publication provides further information on this topic.

Materials and reagents

Policy information about availability of materials

8. Materials availability

Indicate whether there are restrictions on availability of unique materials or if these materials are only available for distribution by a for-profit company.	*Describe any restrictions on availability of unique materials used in the study OR confirm that all unique materials used are readily available from the authors or from standard commercial sources (and specify these sources) OR state that no unique materials were used.*

9. Antibodies

Describe the antibodies used and how they were validated for use in the system under study (i.e. assay and species).	Mouse anti-GAPDH (Millipore, MAB374, clone 6C5). Millipore highly validated antibody with currently 594 citations of use in pubmed. Mouse anti-Nestin (Millipore, MAB353, clone rat-401). Millipore highly validated antibody with currently 174 citations of use in pubmed. Mouse anti-Tuj1/bIII-Tubuilin (Millipore, MAB1637, clone TU-20). Millipore highly validated antibody with currently 126 citations of use in pubmed. Mouse anti-Tuj1/bIII-Tubulin (Santa Cruz Biotechnology, sc-58888). Manufacturer validated and guaranteed for immunocytochemistry, immunohistochemistry, and western blot; with 15 citations on pubmed. Mouse anti-TRA-1-60 (Millipore, MAB4360, clone TRA-1-60). Manufacturer validated and guaranteed for immunofluorescence with 92 citations on pubmed. Mouse anti-TRA-1-81 (Millipore, MAB4381, clone TRA-1-81). Manufacturer validated and guaranteed for immunofluorescence with 75 citations on pubmed. Goat anti-LIN28A (R&D Systems, AF3757). Manufacturer validated and guaranteed for immunocytochemistry with pubmed citations: PMID 28392219, 28912471, 24619130, 21209933, 18035408. Rabbit anti-Oct3/4 (Santa Cruz Biotechnology, sc-9081, H-134). Manufacturer validated and guaranteed for immunofluorescence with 138 citations on pubmed. Rabbit anti-Nanog (Santa Cruz Biotechnology, sc-33760, M-149). Manufacturer validated and guaranteed for immunofluorescence with 18 citations on pubmed. Goat anti-DCX (Santa Cruz Biotechnology, sc-8066, C-18). Manufacturer validated and guaranteed for immunofluorescence. There are 225 citations for this product on pubmed. Goat anti-Sox2 (Santa Cruz Biotechnology, sc-17320, Y-17). Manufacturer validated and guaranteed for immunofluorescence with 119 citations on pubmed. Mouse anti-MAP2 (Millipore, MAB3418, clone AP20). Millipore highly validated antibody with currently 100 citations in pubmed. Mouse anti-BLBP (abcam, ab131137, AT1D1). Manufacturer validated and guaranteed for use in immunohistochemistry, with citation PMID 27729849 in pubmed. Rabbit anti-GFAP (Sigma, G9269). Manufacturer validated and guaranteed for use in immunohistochemistry with 104 citations in pubmed. Rabbit anti-Olig2 (abcam, ab81093). Manufacturer validated and guaranteed for immunofluorescence with 8 references in pubmed. Mouse anti-bCatenin (BD Biosciences, 610153, clone 14). Manufacturer tested and guaranteed for immunofluorescence. Citations: PMID 10629227, 23085754, 12235124, 2349235, 11402061, and 11696557. Rabbit anti-ARL13B (Proteintech, 17711-1-AP). Manufacturer tested and guaranteed for immunofluorescence with 162 citations on pubmed. Rabbit anti-Arp3 (Santa Cruz Biotechnology, sc-15390, H-110). Manufacturer validated and guaranteed for western blot. Citations: PMID 26977009, 23526406, 21146522, 17028176, 16155590, and 14729058. Rabbit anti-DCX (homemade, see PMID 10399933). Mouse anti-Beta-Actin (Sigma, A1978, clone AC-15), which has 2077 citations. It is guaranteed by Sigma for a variety of applications, including western blot. Rabbit anti-EIF3D (Bethyl laboratories, A301-758A), guaranteed for western blot by Bethyl laboratories, and has 4 citations (PMID 28650797, 27462815, 26990993, and 25849773). Rat anti-alphaN-catenin (Developmental Studies Hybridoma Bank, NCAT2) was validated and published PMID: 1638632. In our study, we also show this antibody has no reactivity with CTNNA2 knockout cells but produces a band(s) of correct approximate size by western blot.

10. Eukaryotic cell lines

a. State the source of each eukaryotic cell line used.	Patient derived fibroblasts, reprogrammed to iPSC using episomal-mediated transformation. H9 hESCs were obtained from WiCell.
b. Describe the method of cell line authentication used.	Genotyping was performed in-house and karyotyping was performed by commercial laboratory.
c. Report whether the cell lines were tested for mycoplasma contamination.	All lines were tested for mycoplasma monthly and were always negative
d. If any of the cell lines used are listed in the database of commonly misidentified cell lines maintained by ICLAC, provide a scientific rationale for their use.	N/A except for HEK293T cell lines used to generate lentivirus.

Animals and human research participants

Policy information about studies involving animals; when reporting animal research, follow the ARRIVE guidelines

11. Description of research animals

Provide details on animals and/or animal-derived materials used in the study.	N/A

Policy information about studies involving human research participants

12. Description of human research participants

Describe the covariate-relevant population characteristics of the human research participants.	Patients with cortical pachygyria were recruited from world-wide clinics and assembled collaboratively. Control subjects were either healthy related or unrelated volunteers for genetic and iPSC studies.